RSC Advances

PAPER

View Article Online
View Journal | View Issue

Cite this: *RSC Adv.*, 2026, **16**, 1565

First-principles investigation of transition-metal doped Al_2B_2 and AlB_4 monolayers for spintronics

JueFei Wang * and Xuan Luo

Two-dimensional spintronics has garnered significant attention in recent years, driven by the rapidly increasing demand for greater computational power from machine learning and AI workloads. This research investigates whether substitutional doping with the transition metals Mn, Fe, and Cr induces magnetism in two recently discovered, lightweight, two-dimensional Dirac nodal line semimetal monolayers, Al_2B_2 and AlB_4. Computations performed with density functional theory (DFT) reveal ferromagnetic ground states in nine of the twelve investigated monolayers. Defect formation energy calculations show that substitution on Al sites in both monolayers is thermodynamically preferred over B sites. The opening of gaps at band crossings is observed in band structures across all monolayers when spin–orbit coupling effects are introduced, suggesting nontrivial topologies of the pure materials are most likely retained. These findings identify doped Al_2B_2 and AlB_4 monolayers as promising platforms for the future exploration of two-dimensional spintronics.

Received 28th August 2025
Accepted 17th December 2025

DOI: 10.1039/d5ra06454f

rsc.li/rsc-advances

1. Introduction

The rapid expansion of AI and machine-learning workloads is driving unprecedented demand for higher performance and energy efficiency across modern processor architectures, most notably for CPU and GPU platforms. While efforts continue to be made towards downscaling the dimensions of transistors, physical limitations of current technologies are fast approaching. Factors like the high current resistivity of copper wiring, thermal bottlenecks in silicon wafers, and quantum tunneling issues all present significant challenges, highlighting a growing imperative to explore alternative approaches to information processing.[1–3] Spintronics, or spin transport electronics, has emerged as a compelling candidate for the foundation of future computing platforms, with promises to resolve major current technological roadblocks in the development of faster processors.[4–7] By leveraging the spin degree of freedom, either alone or alongside charge, spintronics devices have the potential to overcome limitations of traditional, charge-only electronics by substantially increasing the nonvolatility, speed, and energy efficiency of next-generation computational systems.[1,4,5,7]

In the past few decades, significant strides have been made in the field of spintronics, starting with the discovery of giant magnetoresistance (GMR) in 1988. GMR spin valves quickly enabled the creation of room-temperature, field-sensitive multilayers that found widespread usage as hard-disk read/write heads.[8–12] MRAM cells were subsequently prototyped using GMR and early magnetic tunneling junction (MTJ) structures.[9,13] Then followed the discovery of dilute magnetic semiconductors (DMS), created by doping non-magnetic semiconductors with magnetic impurities, which offer carrier-mediated magnetism that is able to be manipulated by gate voltage, electric current, and light.[14] Today, spin-transfer-torque MRAMs (STT-MRAM) that employ MTJs are being integrated as embedded nonvolatile memory in automotive, industrial, and consumer electronics SoCs, complementing or altogether replacing embedded Flash and SRAM. These devices offer key benefits like low power consumption, nonvolatility, nanosecond read/write speeds, and excellent scalability to smaller nodes.[15–17] Yet there still exists several roadblocks in the way of translating the usage of current spintronics technology from embedded memory to broader, processor-grade functionality. For instance, STT-MRAMs, the main commercial application of spintronics today with an estimated market worth of several billion dollars, require a large write current density that results in significant power consumption, and can risk damaging the MgO barrier at small diameters.[17–20] In addition, the shared read/write paths of STT-MRAMs make it difficult to optimize both writability and read-disturb margin simultaneously.

Table 1 Electron configurations and radius cutoffs used to generate the PAW pseudopotentials for elements used in the current research

Element	Atomic number	Electron configuration	Radius cutoff (bohr)
Al	13	$[Ne]3s^23p^1$	1.904
B	5	$[He]2s^22p^1$	1.701
Cr	24	$[Ne]3s^23p^64s^13d^5$	2.108
Mn	25	$[Ne]3s^23p^64s^13d^6$	2.112
Fe	26	$[Ne]3s^23p^64s^13d^7$	2.115

National Graphene Research and Development Center, Springfield, Virginia 22151, USA. E-mail: juefei_wang@outlook.com

Widening the width of the access transistor for reliable reads can cause bit flips during normal operation, likewise with thinning the MgO tunnel barrier.[19,21–24] Finally, nearly all STT-MRAM designs rely on single-ended sensing against a fixed reference current, where tiny variations in oxide thickness or barrier uniformity can potentially push valid read currents into ambiguous zones that cannot be accurately read.[19,25,26]

With investigations revealing their potential to bypass many said drawbacks, topological quantum materials—systems with nontrivial band topology and unconventional electronic states protected by topological invariants—have garnered significant interest in the past twenty years for spintronics research. Notably, magnetic topological semimetals (MTSMs) have gained considerable attention due to their unique properties that arise from the interplay between topology and magnetism.[27] Their broken time-reversal symmetries and topological band crossings (isolated Weyl/Dirac nodes or nodal lines) grant them electronic pathways that exhibit chirality and can support channels of perfect conduction. The potential ability to manipulate their topological states *via* magnetism pose an appealing area of research, and MTSMs have been predicted to have a myriad of uses in areas ranging from quantum computing, novel electronics, electromagnetic sensors, energy harvesting, and importantly, spintronics.[28–30]

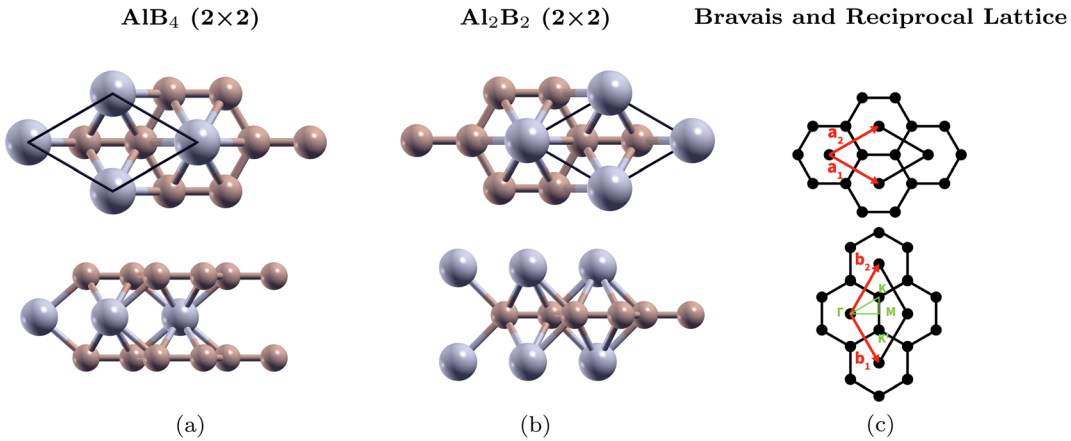

Fig. 1 Top and side views of (a) AlB_4 and (b) Al_2B_2 monolayers in 2 × 2 supercells, and (c) schematic of the Bravais lattice (**a**1, **a**2) and reciprocal lattice (**b**1, **b**2) of the monolayers.

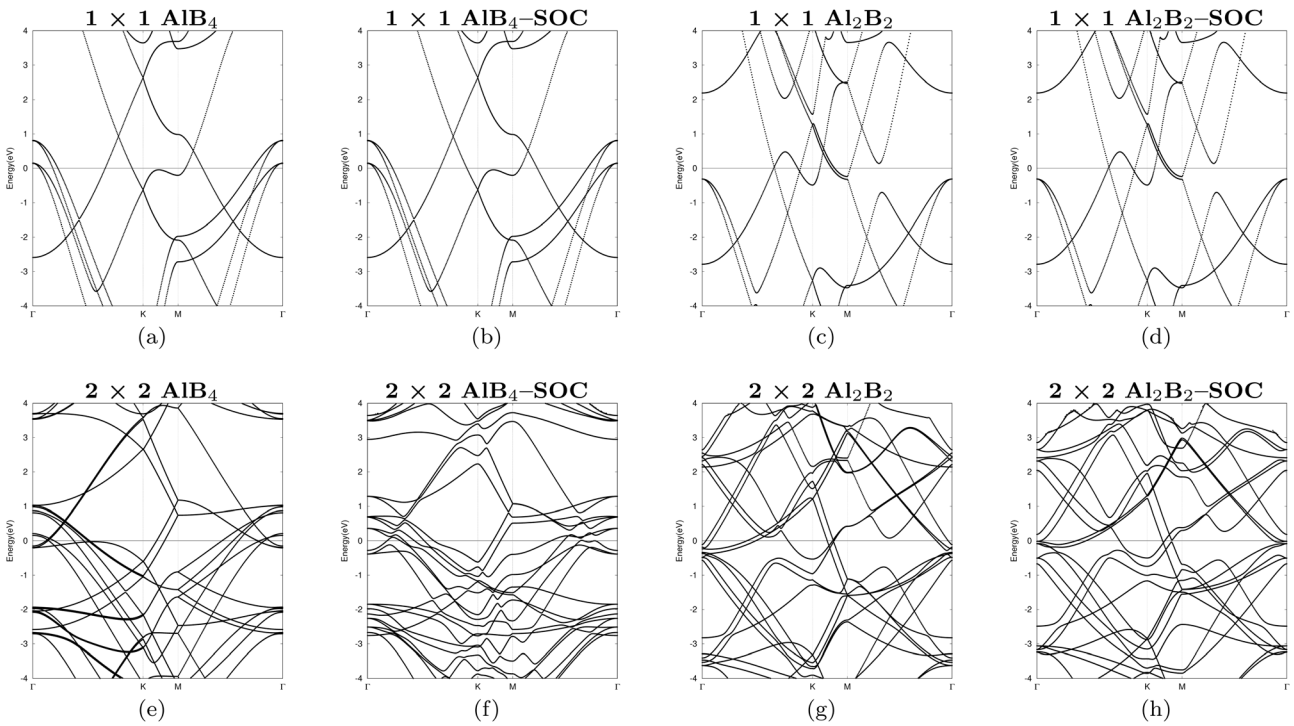

Fig. 2 Electronic band structures (a) and (b) of the primitive cell of AlB_4 without/with SOC and (c) and (d) of the primitive cell of Al_2B_2 without/with SOC. Electronic band structures (e) and (f) of the 2 × 2 supercell of AlB_4 without/with SOC and (g) and (h) of the 2 × 2 supercell of Al_2B_2 without/with SOC. All panels follow the high-symmetry Γ–K–M–Γ *k*-point circuit. The Fermi level is set to 0 eV for all plots.

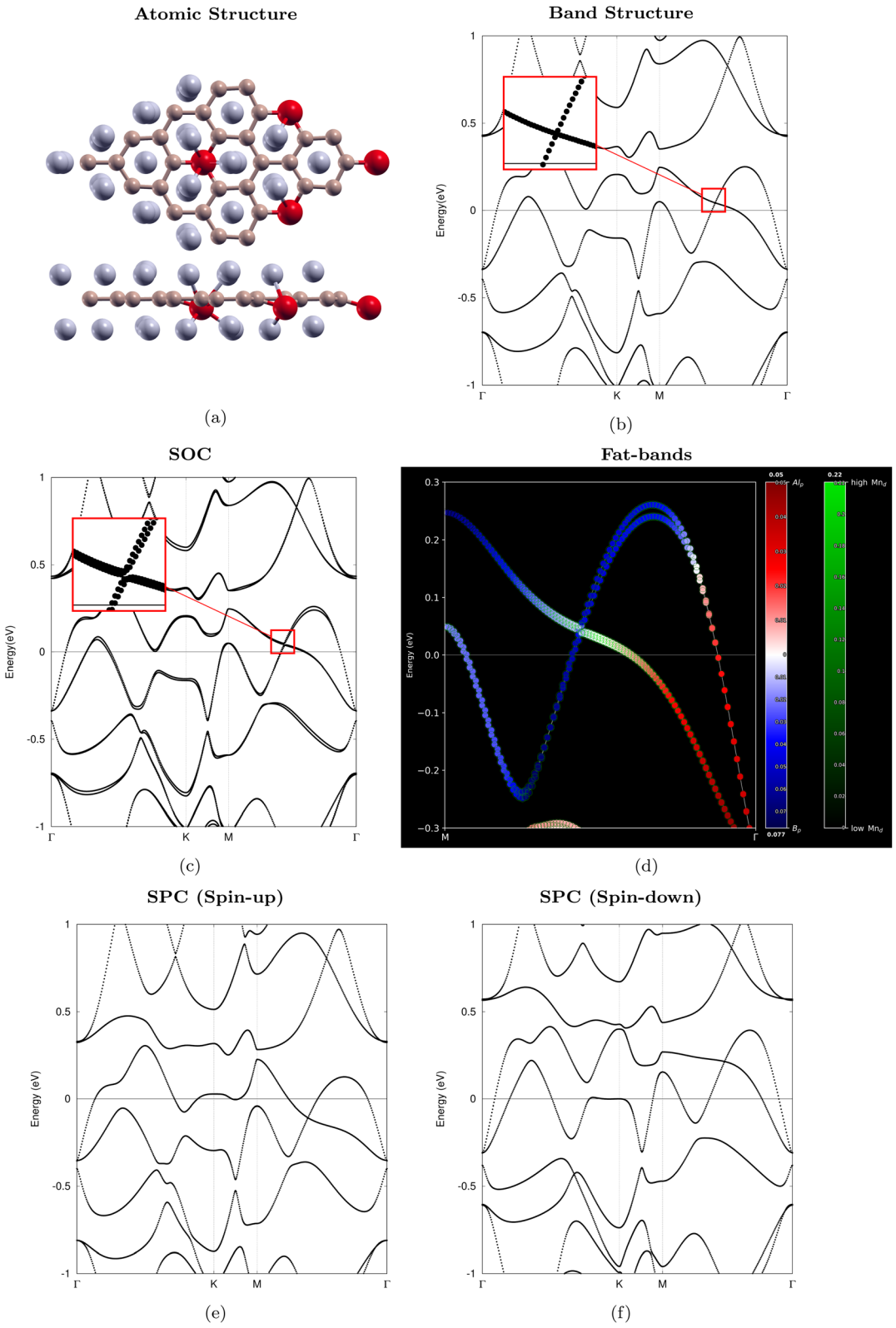

Fig. 3 Mn_B in 2 × 2 Al_2B_2. (a) Top view and side view of the 2 × 2 optimized atomic structure. Beige, gray, and red represent B, Al, and Mn, respectively. (b) Electronic band structure with red inset box. (c) SOC band structure with red inset box. (d) Fat-bands projection on region with gap opening. Red and blue indicate contributions from Al3p and B2p orbitals, respectively. Green outlines represent contributions from Mn3d orbitals. Color bars show absolute orbital-projection values for each channel. (e) and (f) Spin-polarized spin-up and spin-down band structures. All panels follow the high-symmetry Γ–K–M–Γ *k*-point circuit.

Pushing these materials to the two-dimensional limit amplifies their advantages. 2D materials exhibit unique properties like ultra-long spin relaxation times and spin diffusion lengths, allowing efficient transport of spin information.[31–34] They also provide intrinsic avenues for spin manipulation with properties like Rashba spin orbit coupling, spin valley coupling, and quantum spin Hall (QSH) edge channels (currently at up to 100 K).[34–38] The unique dimensionality of these materials has allowed them to realize architectures with decoupled read/write paths, atomically uniform tunnel barriers, and nonvolatile electric control of magnetism, which lowers power consumption.[26,39–41] Amongst these materials, 2D MTSMs, which exhibit both enhanced magnetic anisotropy and quantum confinement effects not observed in any bulk material, offer a particularly fascinating direction of research for applications in spintronics.[42,43] Particularly since the experimental realization of graphene, followed by successful discoveries and productions of monolayers like silicene, hexagonal hBN, and TMDs, significant interest arose in their research.[44–46] Nonetheless, despite considerable efforts that have been made in recent years, the interactive nature of MTSMs make them hard to predict, and there have thus been few newly reported discoveries. There are, however, some notable exceptions like $Sr_{1-y}Mn_{1-z}Sb_2$ ($y, z < 0.1$), Fe_3GeTe_2, and the pressure-induced $EuCd_2As_2$.[47–53] These successfully discovered materials all display considerable potential through either their topological characteristics or spintronics applications, underscoring the value of continued exploration.

Taken together, these limitations and opportunities motivate our investigation of lightweight, 2D topological materials and whether magnetic doping can unlock spintronics functionalities in them while retaining topology. Al_2B_2 and AlB_4 monolayers, two 2D Dirac nodal line semimetals predicted by Abedi *et al.* in 2022, have drawn scientific interest due to their potential applications in future quantum and nanoscale devices, especially in the case of the 2D superconductor AlB_4.[51] These monolayers have also demonstrated promise in other applications like sodium-ion batteries.[54] However, their spintronics potential remains largely unexplored. This, with the addition of nascent research on the doping of topological monolayers, motivated us to explore the possibility of introducing impurities to these materials with transition metal dopants in search of magnetism and therefore potential uses in spintronics.[55–58] Other modifications, such as layer stacking, strain engineering, and carrier or chemical doping, have also been employed to induce spintronic functionality in 2D systems.[59–61] Nevertheless, we focus on transition-metal doping because it provides a direct and experimentally established route to introduce localized magnetic moments while largely preserving the symmetry-protected topological features of Al_2B_2 and AlB_4.

Importantly, the experimental feasibility of such doping strategies has been demonstrated in related 2D materials. For instance, substitutional transition metal doping *via* chemical vapor deposition (CVD) has been widely used in two-dimensional semiconductors. CVD growth enables incorporation of dopant precursors during synthesis, allowing, *e.g.*, transition metal-doped TMD monolayers.[62,63] Moreover, a microwave-assisted one-pot method was used to dope the 12-borophene phase with Fe and S by exposing dispersed borophene to $FeCl_3$ under controlled microwave irradiation; this work achieved up to 13% Fe doping, as confirmed by high-resolution transmission electron microscopy (HRTEM) and Raman spectroscopy.[64] Additional postgrowth techniques, such as low-energy ion implantation, have been applied to 2D materials like few-layer WS_2, allowing precise control of dopant concentration. The universality of this method has also been demonstrated in other 2D semiconductors, including WSe_2, SnS_2, and MoS_2. These experimental successes offer compelling evidence that the substitutional doping schemes we explore are realistic and could be implemented in the laboratory.

In this paper, we describe our procedures in using first-principles calculations based on DFT to demonstrate the emergence of magnetism across Al_2B_2 and AlB_4 monolayers after doping them with several common transition metals. We also explore the possibility that these materials retain topological properties similar to their pristine counterparts. We detail the structural and magnetic properties of these systems, and discuss possible implementations in 2D spintronics and potentially as MTSMs. In Section 2, we detail our methods of performing first-principles calculations. In Section 3, we present and discuss our results for both materials. Finally, our conclusion and framework for future directions is found in Section 4.

2. Method

2.1. Computational details

First-principles calculations were performed based on Density Functional Theory (DFT) using the Generalized Gradient Approximation (GGA) in a Perdew–Burke–Ernzerhof (PBE) formalism as implemented in the ABINIT[65] code. The Projector Augmented-Wave (PAW) method[66] was used to generate pseudopotentials by the ATOMPAW code.[67] Table 1 displays the electron configurations and radial cutoffs of the elements used to conduct our study.

Total energies were computed *via* self-consistent field (SCF) convergence. Cycles were terminated once the total energy difference between two successive iterations was smaller than 1×10^{-10} Ha. The kinetic energy cutoff, vacuum parameters, and Monkhorst–Pack k-point grid were converged until the total energy differences were less than 1×10^{-4} Ha twice consecutively. To optimize atomic structure, the Broyden–Fletcher–Goldfarb–Shanno (BFGS) minimization algorithm was used such that the maximum absolute force difference was less than 2×10^{-4} Ha bohr^{-1} between two consecutive runs.

2.2. Atomic structure

As shown in Fig. 1(a) and (b), the primitive cells of the pure Al_2B_2 and AlB_4 monolayers are hexagonal lattices of the layer

Table 2 Defect formation energies E_f^{Mn} of doped Al_2B_2 and AlB_4 monolayers, their fully relaxed in-plane lattice constants, and total magnetic moment

Material	Defect	E_f^{Mn} (Ha)	In-plane latt. (bohr)	Magnetic moment (μ_B)
Al_2B_2	D_B	0.237	11.522	0.677
Al_2B_2	D_{Al}	0.003	11.023	3.765
AlB_4	D_B	0.199	11.369	2.101
AlB_4	D_{Al}	−0.023	11.208	2.193

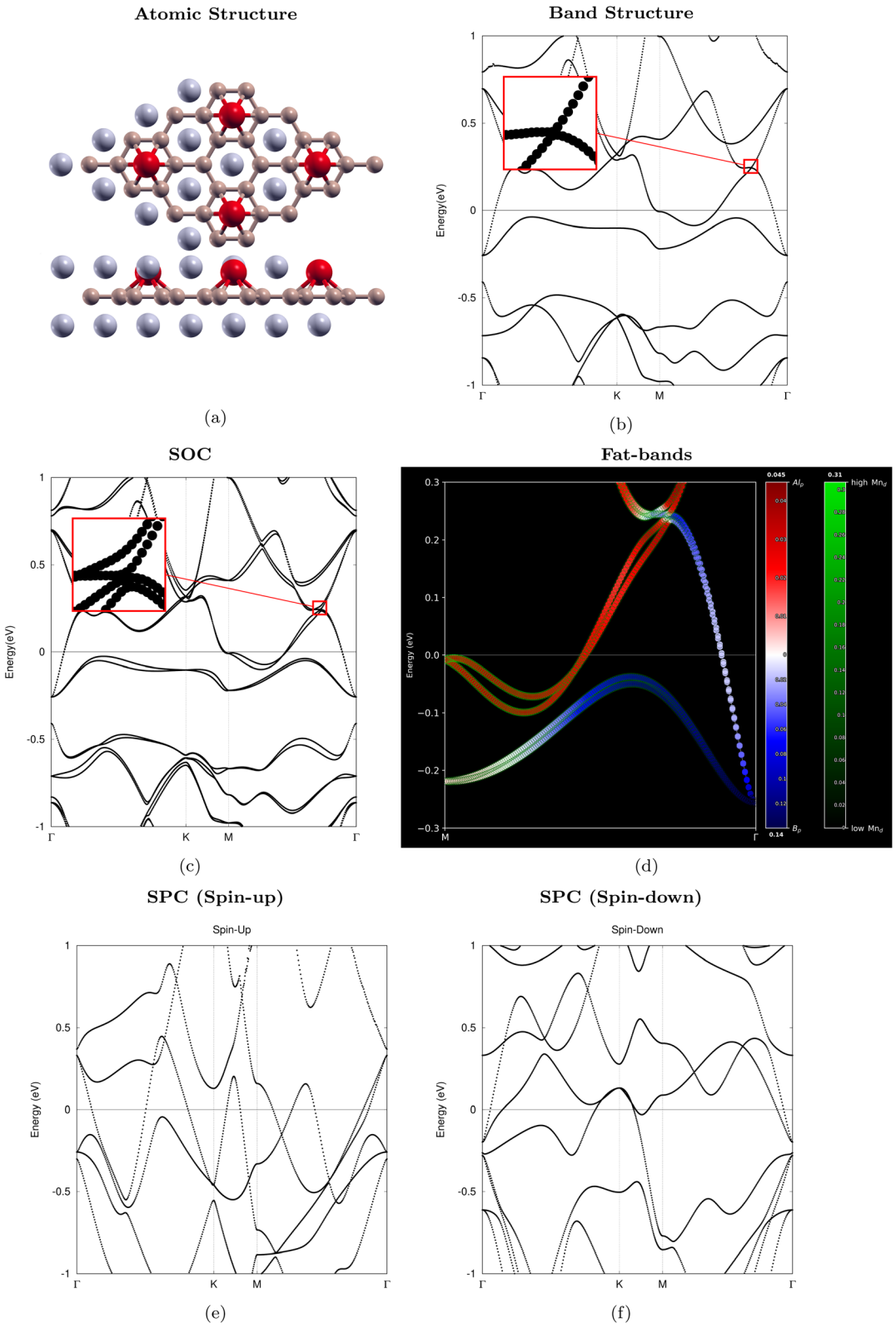

Fig. 4 Mn_{Al} in 2 × 2 Al_2B_2. (a) Top view and side view of the 2 × 2 optimized atomic structure. Beige, gray, and red represent B, Al, and Mn, respectively. (b) Electronic band structure with red inset box. (c) SOC band structure with red inset box. (d) Fat-bands projection on region with gap opening. Red and blue indicate contributions from Al3p and B2p orbitals, respectively. Green outlines represent contributions from Mn3d orbitals. Color bars show absolute orbital-projection values for each channel. (e) and (f) Spin-polarized spin-up and spin-down band structures. All panels follow the high-symmetry Γ–K–M–Γ *k*-point circuit.

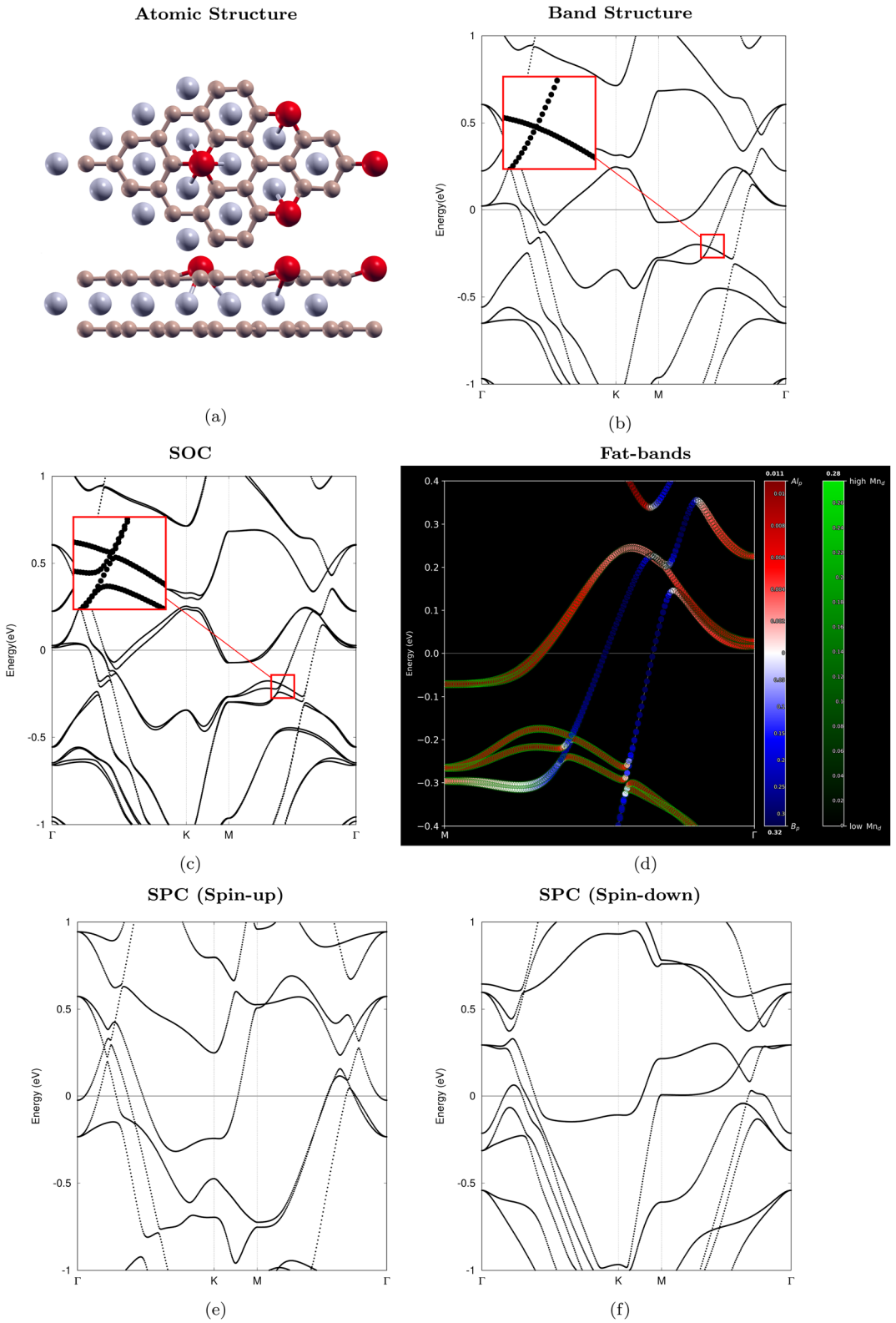

Fig. 5 Mn_B in 2 × 2 AlB_4. (a) Top view and side view of the 2 × 2 optimized atomic structure. Beige, gray, and red represent B, Al, and Mn, respectively. (b) Electronic band structure with red inset box. (c) SOC band structure with red inset box. (d) Fat-bands projection on region with gap opening. Red and blue indicate contributions from Al3p and B2p orbitals, respectively. Green outlines represent contributions from Mn3d orbitals. Color bars show absolute orbital-projection values for each channel. (e) and (f) Spin-polarized spin-up and spin-down band structures. All panels follow the high-symmetry Γ–K–M–Γ *k*-point circuit.

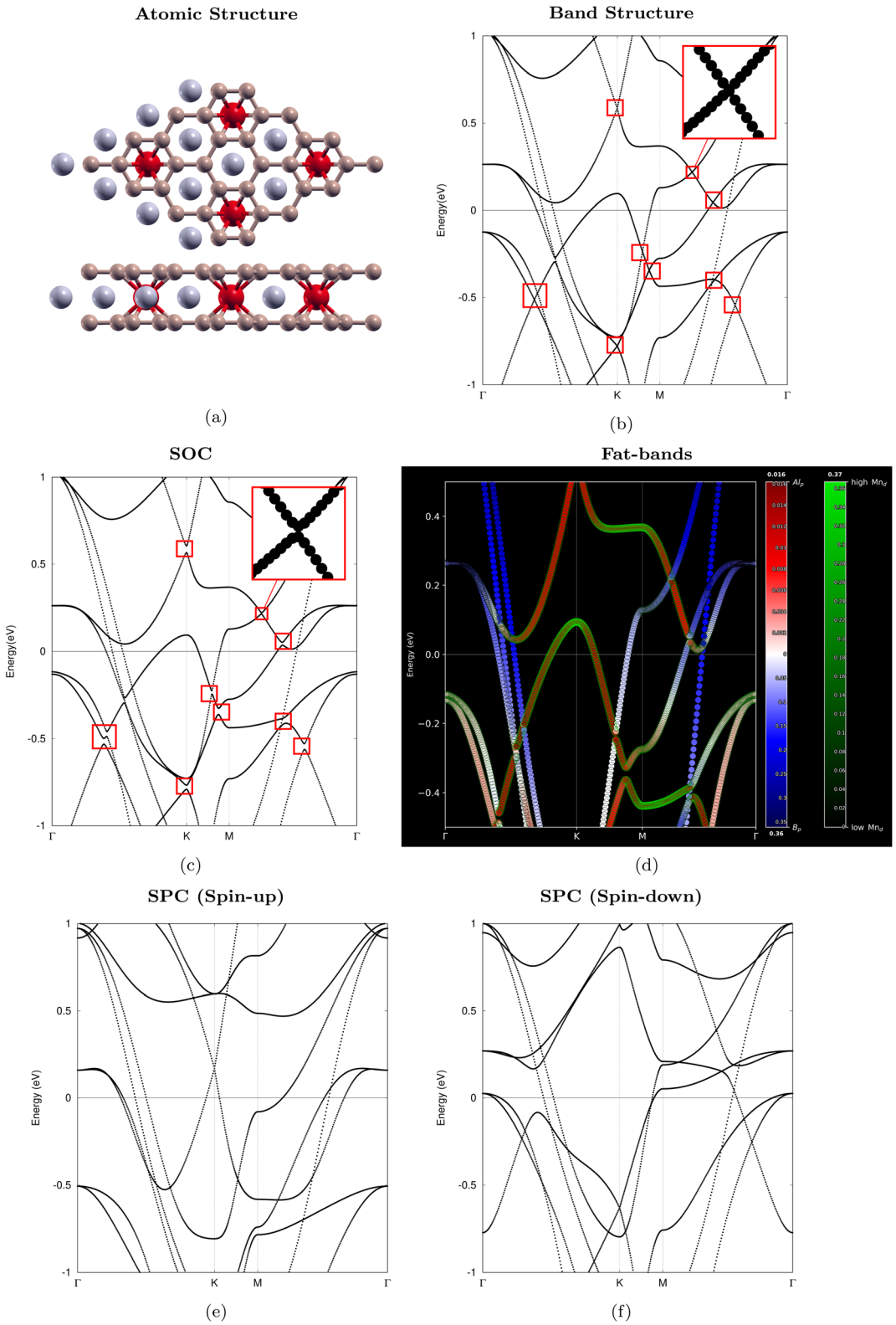

Fig. 6 Mn_{Al} in 2 × 2 AlB_4. (a) Top view and side view of the 2 × 2 optimized atomic structure. Beige, gray, and red represent B, Al, and Mn, respectively. (b) Electronic band structure with red inset box. (c) SOC band structure with red inset box. (d) Fat-bands projection on region with gap opening. Red and blue indicate contributions from Al3p and B2p orbitals, respectively. Green outlines represent contributions from Mn3d orbitals. Color bars show absolute orbital-projection values for each channel. (e) and (f) Spin-polarized spin-up and spin-down band structures. All panels follow the high-symmetry Γ–K–M–Γ *k*-point circuit.

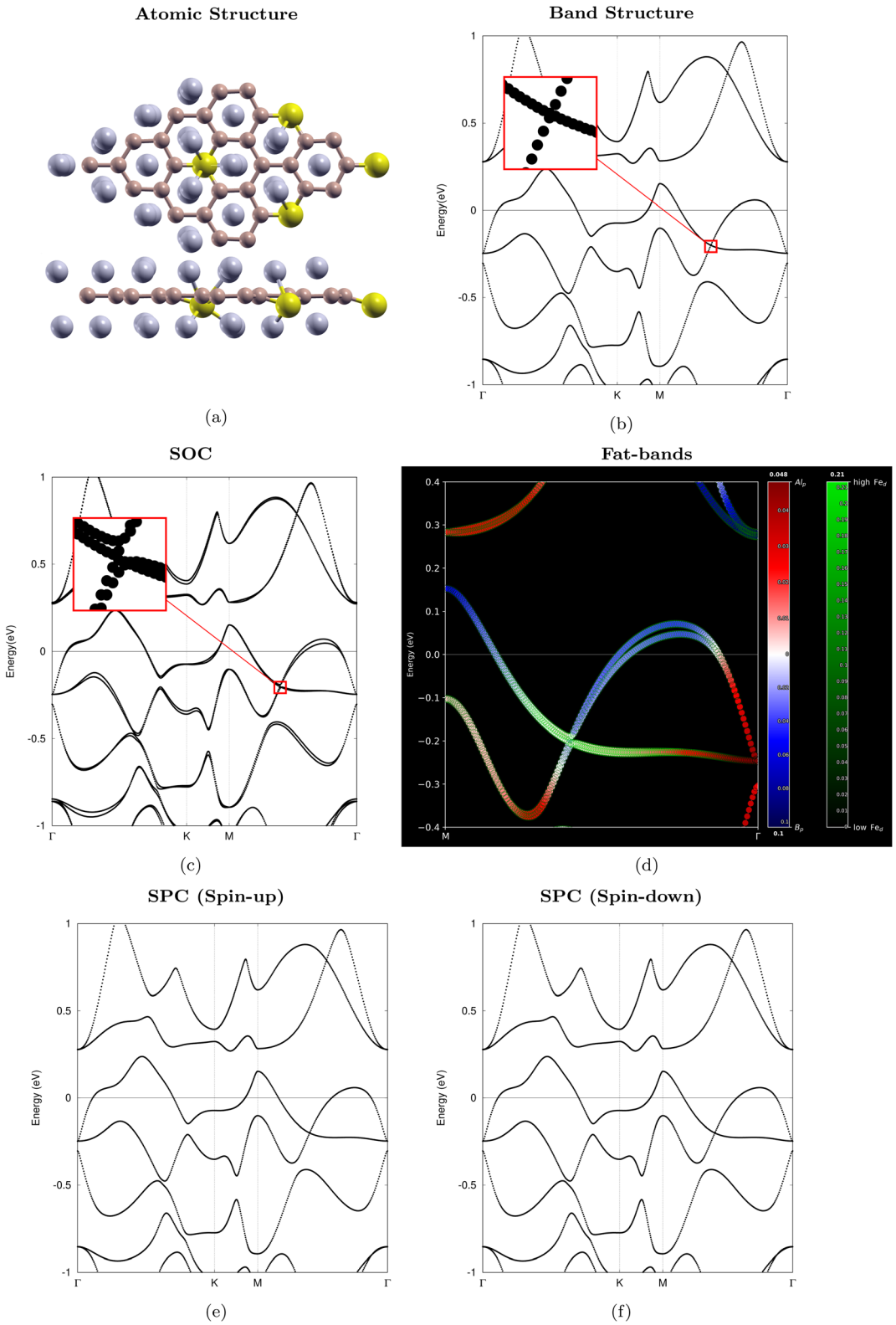

Fig. 7 Fe_B in 2 × 2 Al_2B_2. (a) Top view and side view of the 2 × 2 optimized atomic structure. Beige, gray, and yellow represent B, Al, and Fe, respectively. (b) Electronic band structure with red inset box. (c) SOC band structure with red inset box. (d) Fat-bands projection on region with gap opening. Red and blue indicate contributions from Al3p and B2p orbitals, respectively. Green outlines represent contributions from Fe3d orbitals. Color bars show absolute orbital-projection values for each channel. (e) and (f) Spin-polarized spin-up and spin-down band structures. All panels follow the high-symmetry Γ–K–M–Γ k-point circuit.

group P6/*mmm* (no. 80). These two configurations give rise to the thinnest AlB_2 films, and share similar structures when viewed top-down. They are, however, distinct in their side views. The starting geometries we used in our study were taken from prior calculations reported by Abedi *et al.* in 2022.[51]

2.3. Electronic structure

The band structures of the monolayers were calculated along the Γ–K–M–Γ path in the two-dimensional Brillouin zone. In reduced coordinates of the reciprocal primitive lattice, the high-symmetry *k*-points are Γ (0, 0, 0), K (1/3, 2/3, 0), and M (1/2, 1/2, 0) (Fig. 1(c)).

Subsequently, spin–orbit coupling (SOC) effects were introduced while all other computational parameters were kept unchanged, enabling a one-to-one comparison with the scalar-relativistic bands.

Band gaps produced by this lifting of spin degeneracies were further examined using orbital-projected (fat-bands) plots with SOC to inspect contributions from different orbitals.

To identify whether magnetism exists in the ground state, spin-polarized calculations (SPC) were conducted *via* the assignment of initial local moments. Full structural relaxation was then re-performed, followed by a re-calculation of the band structures with separate spin-up and spin-down channels.

2.4. Defect formation energies

To evaluate the defect formation energies of our doped monolayers, of which all are neutral defects, we use the following formula, analogous to ones employed in similar studies:[68–70]

$$E_f(D) = E_{tot}(\text{defect}) - E_{tot}(\text{host}) - \sum_i n_i \mu_i \quad (1)$$

Here, E_{tot}(defect) and E_{tot}(host) are the Helmholtz free energies of the system with and without the defect, n_i is the number of atoms of species added or removed, and μ_i is their corresponding chemical potentials. At $T = 0$ K we approximate Helmholtz free energy as equal to total energy. In our study, all dopings are performed *via* the substitution of one atom of either Al or B with a dopant. As such, the equation simplifies to

$$E_f(D_X) = E_{D_X} - E_{ML} - E_D + E_X, \quad \text{with } D \in \{Mn, Fe, Cr\}, \; X \in \{B, Al\}, \; ML \in \{AlB_4, Al_2B_2\}. \quad (2)$$

3. Results and discussion

We examine the electronic structures of the pure monolayers, then investigate the defect formation energies for substitutional doping with Mn, Cr, and Fe. Then, we present a dopant-by-dopant study of the magnetic and topological properties of the monolayers by evaluating the fully relaxed band structures, SOC, SPC, and fat-bands.

3.1. Pure monolayers

To establish a baseline for evaluating the effects of transition metal doping on the monolayers, we start by examining the structural and electronic properties of pristine Al_2B_2 and AlB_4 monolayers. Following the metrics detailed in Section 2, we first performed kinetic energy convergence, followed by the convergence of Monkhorst–Pack *k*-point grid, then vacuum height, and finally full structural relaxation at 0 GPa.

Following this, the in-plane lattice constants of the monolayers were determined to be 5.566 bohr for Al_2B_2 and 5.695 bohr for AlB_4. These results are in excellent agreement with the theoretical values given by Abedi *et al.*, at 5.573 bohr and 5.658 bohr, for their respective monolayers.[51]

The optimized band structures of the primitive cells of AlB_4 and Al_2B_2 are as presented in Fig. 2. After consideration of SOC, the primitive cells yielded no distinguishable differences in band structure, confirming that SOC induces no observable splitting or gap opening in the base material. This is an expected outcome, as both aluminum and boron are light elements with low-Z atoms, and their inversion ($\mathcal{P}$) and time-reversal ($\mathcal{T}$) symmetries enforce a two-fold degeneracy at every *k*-point.

As all doping calculations in this study are performed on 2×2 supercells, we also computed band structures for the fully relaxed supercells of the pristine monolayers to provide *a* point of direct comparison. The supercells relaxed to 11.132 bohr for Al_2B_2 and 11.369 bohr for AlB_4. As we see in Fig. 2, the introduction of SOC effects to these systems produced gap openings across numerous points for both monolayers. These results arise from the lowering of crystal symmetry upon relaxation, lifting the $\mathcal{PT}$ constraints that enforce degeneracy in the primitive cells.

As the following sections show, the introduction of SOC and SPC effects result in significant changes to the band dispersions of graphs produced. The results reveal the emergence of magnetic behavior in Mn_B, Mn_{Al}, Fe_{Al}, and Cr_{Al} in 2×2 Al_2B_2, and for Mn_B, Mn_{Al}, Fe_{Al}, Cr_B, and Cr_{Al} in 2×2 AlB_4. The possibility that the doped systems retain topological features present in the pure material is also observed. Below, we will discuss our reasonings for these assessments through a dopant-by-dopant discussion.

3.2. Mn doped monolayers

In our study of the doped monolayers, we follow the same workflow as we have used for the calculations of the pure material, starting from a full structural relaxation on the dopants after Mn is introduced. Presented in Fig. 3 are the top and side views of the optimized atomic structures of Al_2B_2 with substitutional Mn doping at the B site. The colors beige, gray and red represents B,

Table 3 Defect formation energies E_f^{Fe} of doped Al_2B_2 and AlB_4 monolayers, their fully relaxed in-plane lattice constants, and total magnetic moment

Material	Defect	E_f^{Fe} (Ha)	In-plane latt. (bohr)	Magnetic moment (μ_B)
Al_2B_2	D_B	0.205	11.521	0.000
Al_2B_2	D_{Al}	0.000	11.014	2.648
AlB_4	D_B	0.172	11.382	0.000
AlB_4	D_{Al}	−0.025	11.221	1.030

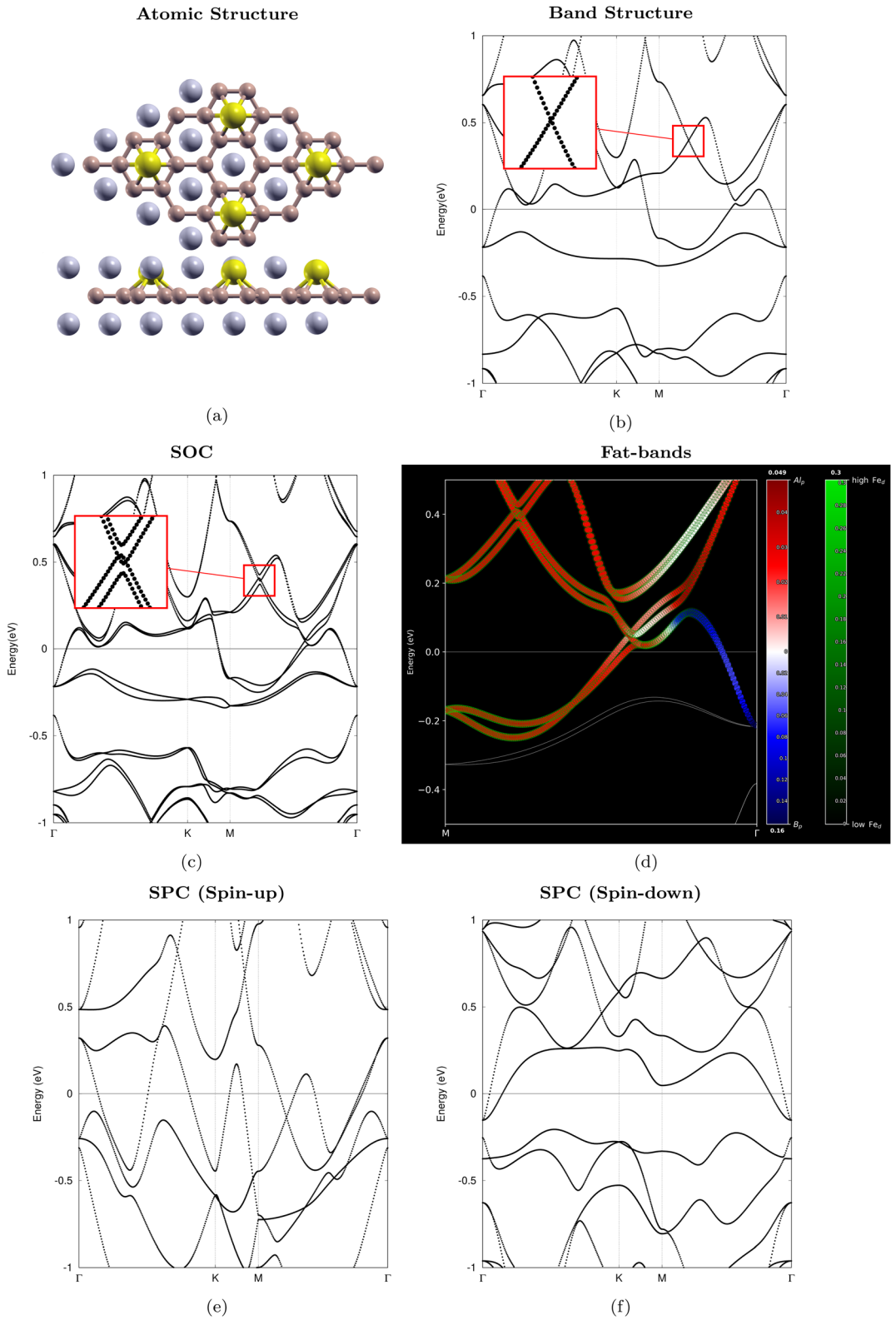

Fig. 8 Fe_{Al} in 2 × 2 Al_2B_2. (a) Top view and side view of the 2 × 2 optimized atomic structure. Beige, gray, and yellow represent B, Al, and Fe, respectively. (b) Electronic band structure with red inset box. (c) SOC band structure with red inset box. (d) Fat-bands projection on region with gap opening. Red and blue indicate contributions from Al3p and B2p orbitals, respectively. Green outlines represent contributions from Fe 3d orbitals. Color bars show absolute orbital-projection values for each channel. (e) and (f) Spin-polarized spin-up and spin-down band structures. All panels follow the high-symmetry Γ–K–M–Γ *k*-point circuit.

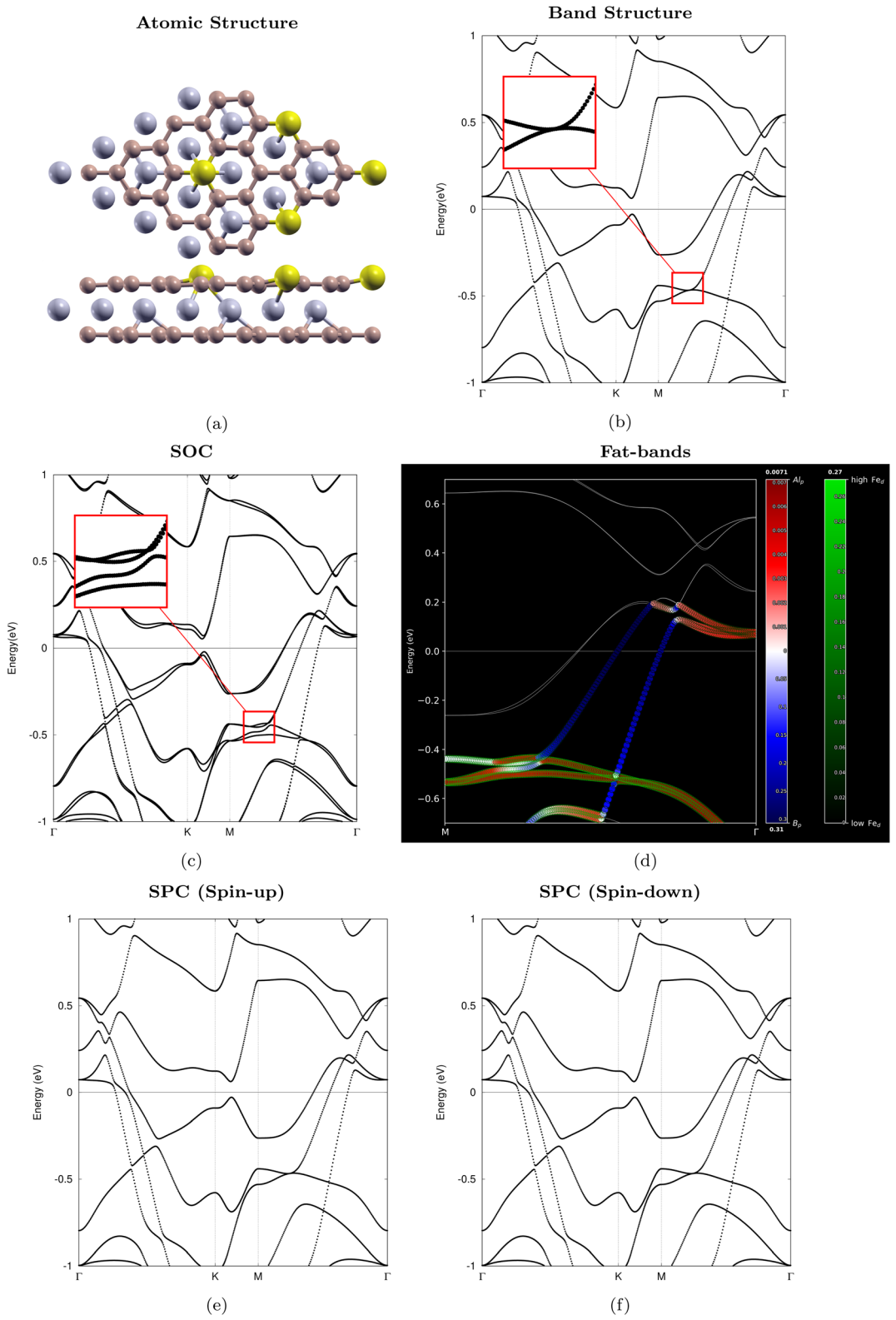

Fig. 9 Fe_B in 2 × 2 AlB_4. (a) Top view and side view of the 2 × 2 optimized atomic structure. Beige, gray, and yellow represent B, Al, and Fe, respectively. (b) Electronic band structure with red inset box. (c) SOC band structure with red inset box. (d) Fat-bands projection on region with gap opening. Red and blue indicate contributions from Al3p and B2p orbitals, respectively. Green outlines represent contributions from Fe3d orbitals. Color bars show absolute orbital-projection values for each channel. (e) and (f) Spin-polarized spin-up and spin-down band structures. All panels follow the high-symmetry Γ–K–M–Γ k-point circuit.

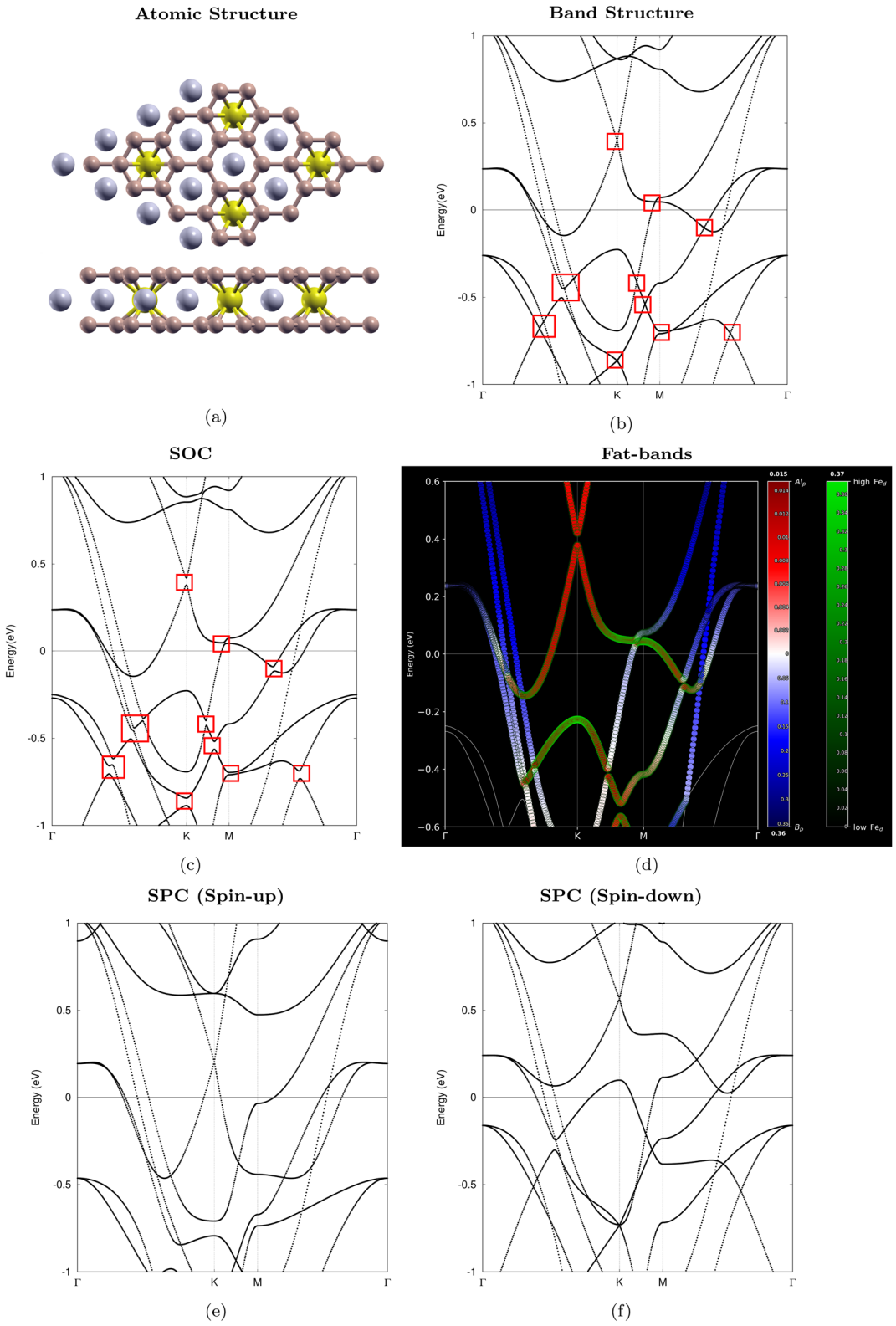

Fig. 10 Fe_{Al} in 2 × 2 AlB_4. (a) Top view and side view of the 2 × 2 optimized atomic structure. Beige, gray, and yellow represent B, Al, and Fe, respectively. (b) Electronic band structure with red inset box. (c) SOC band structure with red inset box. (d) Fat-bands projection on region with gap opening. Red and blue indicate contributions from Al3p and B2p orbitals, respectively. Green outlines represent contributions from Fe3d orbitals. Color bars show absolute orbital-projection values for each channel. (e) and (f) Spin-polarized spin-up and spin-down band structures. All panels follow the high-symmetry Γ–K–M–Γ k-point circuit.

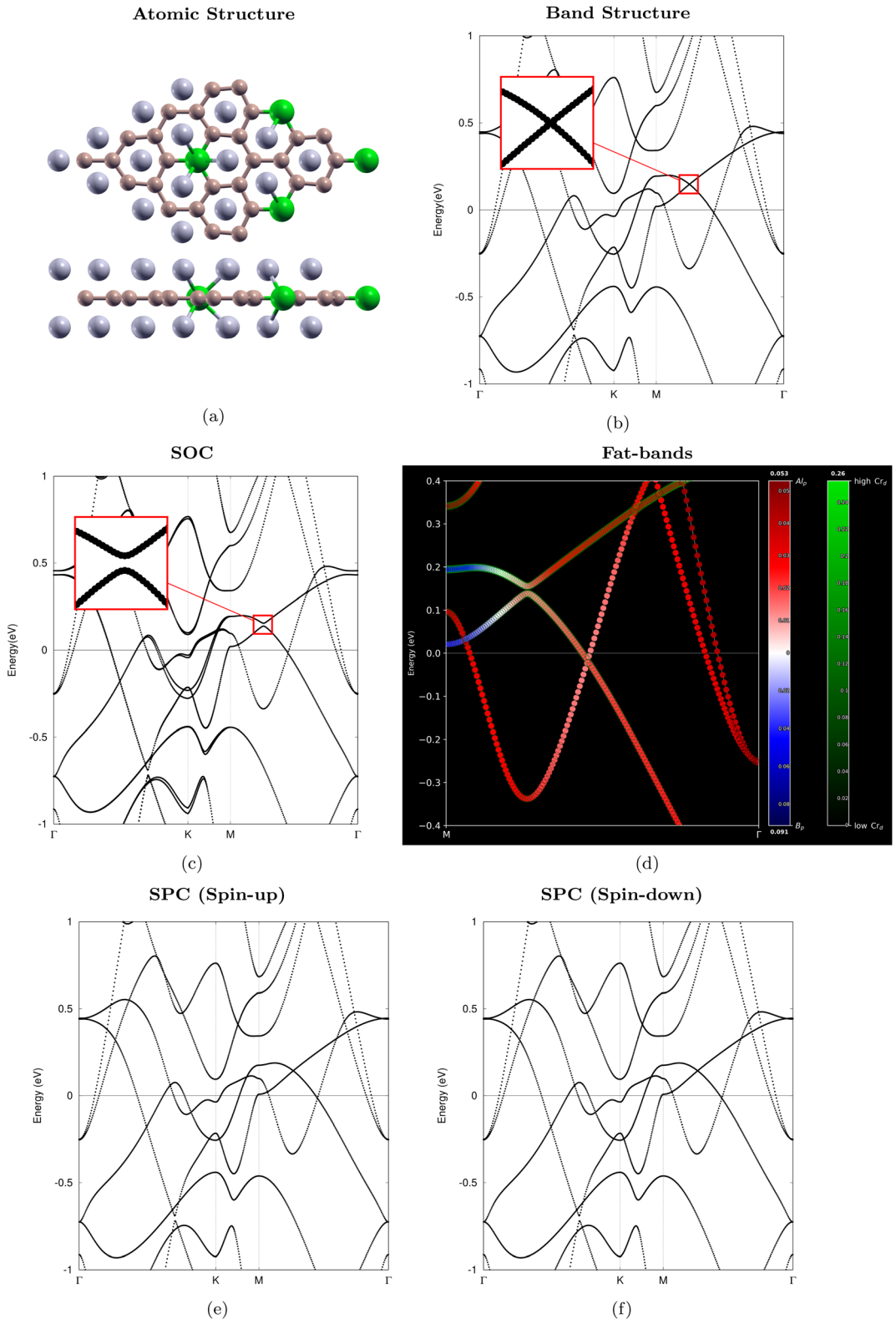

Fig. 11 Cr_B in 2 × 2 Al_2B_2. (a) Top view and side view of the 2 × 2 optimized atomic structure. Beige, gray, and green represent B, Al, and Cr, respectively. (b) Electronic band structure with red inset box. (c) SOC band structure with red inset box. (d) Fat-bands projection on region with gap opening. Red and blue indicate contributions from Al3p and B2p orbitals, respectively. Green outlines represent contributions from Cr3d orbitals. Color bars show absolute orbital-projection values for each channel. (e) and (f) Spin-polarized spin-up and spin-down band structures. All panels follow the high-symmetry Γ–K–M–Γ k-point circuit.

Al, and Mn atoms, respectively. Shown in Table 2, the corresponding in-plane lattice parameter is 11.522 bohr, revealing an increase of 3.50% relative to the pure monolayer. Comparing the band structures of Fig. 3(b) and (c), we observe that the introduction of spin–orbit interactions result in the lifting of degeneracies near the Fermi level along the M–Γ path and opens up a band gap. The ability of SOC effects to gap the band crossing is suggestive of nontrivial topology.[71–73] In Fig. 3(d), red and blue dots respectively display the relative orbital contributions of Al3p and B2p, while green outlines correspond to the strength of the contributions of the dopant, in this case being Mn3d. The bars on the right map color intensity to raw, unitless orbital-projection weights, with the bold markers indicating maximum values. As such, it shows that the orbital weights of Mn3d in the area overpowers that of Al3p and B2p, playing an important role in inducing the gap. Under spin-polarized effects, the spin-up and spin-down band structures differ, as revealed in Fig. 3(e) and (f). Table 2 displays the magnetic moment, calculated by taking the difference between spin-up and spin-down electron counts, integrated over the supercell. Here, the non-zero value confirms the emergence of magnetism.

For Mn_{Al} substitution, we observe that introducing SOC effects again opens up a crossing along the M–Γ path of the band structure, slightly above the Fermi level (Fig. 4(c)). Table 2 presents a 0.98% decrease in the in-plane lattice constant of the doped material in comparison with the pristine monolayer, from 11.132 bohr to 11.023 bohr. The fat-bands plot of Fig. 4(d) reveal that just as in Mn_B doping, the role of the dopant is significant in lowering symmetry and creating the gap. In addition, there is also more Al3p contribution than B2p contribution at the Fermi level. Similar to Mn_B, the spin-up and spin-down differ when SPC is introduced (Fig. 4(e) and (f)). In this case, Table 2 reveals a large total magnetic moment, indicative of a strongly spin-polarized ground state (Table 2).

In the AlB_4 monolayer with B site substitution, there is another appearance of a band opening along the M–Γ path, this time located slightly below the Fermi level, as seen in Fig. 5(c). Interestingly, the lattice constants of this monolayer is identical to that of the pure material, suggestive of there being minimal global strain (Table 2). At the site of the gap, bright green circle outlines indicate significant Mn3d contribution, especially on bands with stronger Al3p relative orbital contributions. From the bars, we also observe that B2p and Mn3d have greater absolute weights in these bands, indicative of their prominent contributions near the Fermi level. In Fig. 5(e) and (f), strong magnetism is once again revealed by the markedly distinct spin-up and spin-down bands, as corroborated by Table 2.

Lastly, in the AlB_4 monolayer with Al site substitution, the in-plane lattice constant is calculated to be 11.208 bohr, corresponding to a 1.42% decrease (Table 2). Numerous nodal points open in the band structure under the influence of SOC, as indicated by the red inset boxes in Fig. 6(b) and (c). Observing Fig. 6(c), it can be seen that across all gaps near the Fermi level, there are strong influences of the Mn3d orbital, particularly in regions with greater Al3p contribution. Similar to AlB_4 with Mn_B substitution, B2p and Mn3d orbitals have greater absolute weights in these bands. As with the three cases above, SPC bands and Table 2 reveal the continuation of the pattern of emergent magnetism (Fig. 6(e) and (f)).

From Table 2, it is clear that substitutions of the Al site has lower formation energies than substitutions of the B site. This is consistent with the structural signatures we observe. Al site doping reduces the in-plane lattice constants of the monolayers, resulting in chemical compressive pressure, whereas B site doping either maintains or expands the lattice constants, resulting in little pressure change in the former scenario and tensile pressure for the latter. The slightly negative defect formation energy of AlB_4 MnAl signifies that even after accounting for the energy needed for vacancy formation, the final doped structure still lowers the net total energy. These results are unsurprising, as there is a better size match between Mn and Al, therefore making it easier to perform doping.

3.3. Fe doped monolayers

Having examined the structural and electronic signatures of Mn substitution and successfully identifying magnetism, we now shift our attention to an adjacent element, Fe, to test whether the same trends persist. As such, we follow the same workflow used above.

Fig. 7(a) shows the top and side views of the optimized atomic structures of Al_2B_2 with substitutional Fe_B doping; yellow represents Fe atoms. The lattice constant, 11.521 bohr, found in Table 3, signify a 3.49% increase compared to the pure Al_2B_2 monolayer. We observe a splitting slightly below the Fermi level along the M–Γ path by comparing Fig. 7(b) to (c). The fat-bands plot and bars reveal that at the Fermi level, B2p dominates over Fe3d, both in terms of relative orbital contributions as well as absolute weights. A high amount of Fe3d character is present at the site of the gapped band crossing (Fig. 7(d)). Interestingly, from the identical looking graphs of Fig. 7(e) and (f), it is apparent that this doped monolayer induces no magnetism, unlike the ones examined previously. This is supported by the zero in the total magnetization column found in Table 3.

A nodal point along the M–Γ path opens when SOC is introduced to Al_2B_2 with Fe_{Al} doping, as shown in Fig. 8(c). Table 3 indicates a 1.06% decrease of the in-plane lattice constant compared to the pure monolayer, from 11.132 to 11.014 bohr. Fig. 8(d), the fat-bands graph, reveal that this opening results from the mixing of Al3p and Fe3d orbitals, with the dopant Fe3d having the greatest absolute weight near the Fermi level. This time, Fig. 8(e), (f) and Table 3 reveal that magnetism is once again found.

Table 4 Defect formation energies E_f^{Cr} of doped Al_2B_2 and AlB_4 monolayers, their fully relaxed in-plane lattice constants, and total magnetic moment

Material	Defect	E_f^{Cr} (Ha)	In-plane latt. (bohr)	Magnetic moment (μ_B)
Al_2B_2	D_B	0.289	11.519	0.000
Al_2B_2	D_{Al}	0.008	11.054	2.668
AlB_4	D_B	0.221	11.363	1.607
AlB_4	D_{Al}	−0.018	11.209	1.813

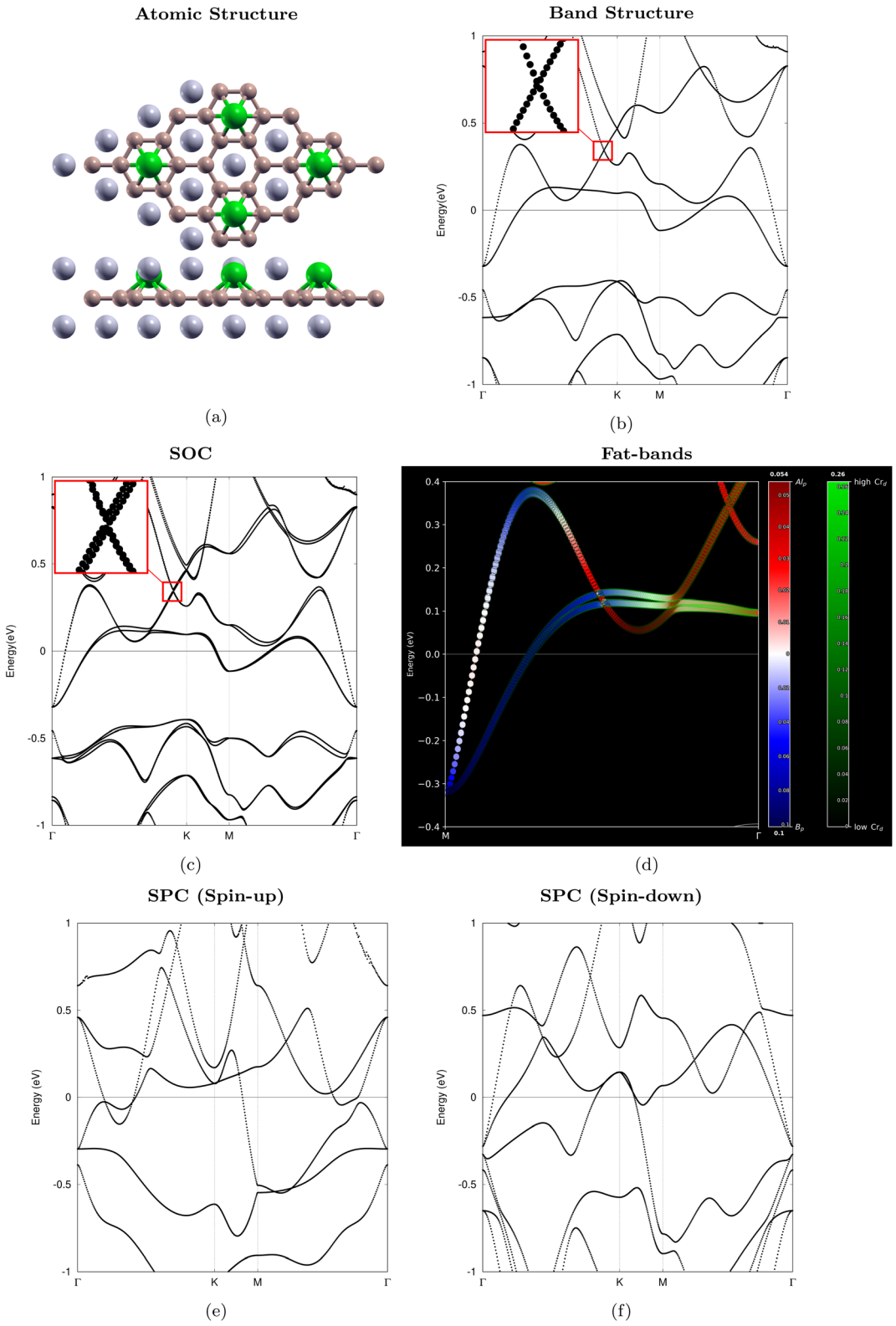

Fig. 12 Cr_{Al} in 2 × 2 Al_2B_2. (a) Top view and side view of the 2 × 2 optimized atomic structure. Beige, gray, and green represent B, Al, and Cr, respectively. (b) Electronic band structure with red inset box. (c) SOC band structure with red inset box. (d) Fat-bands projection on region with gap opening. Red and blue indicate contributions from Al3p and B2p orbitals, respectively. Green outlines represent contributions from Cr3d orbitals. Color bars show absolute orbital-projection values for each channel. (e) and (f) Spin-polarized spin-up and spin-down band structures. All panels follow the high-symmetry Γ–K–M–Γ k-point circuit.

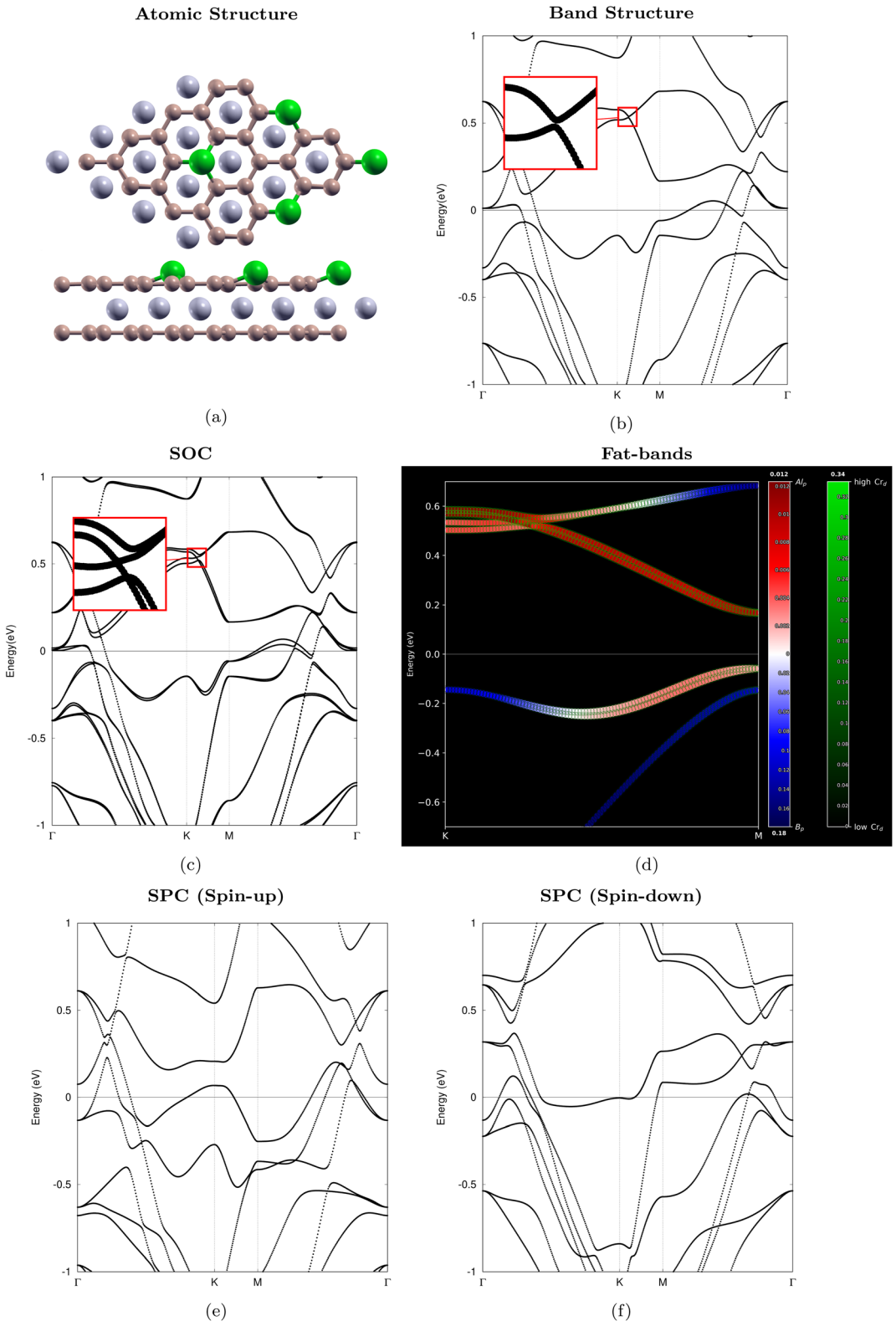

Fig. 13 Cr_B in 2 × 2 AlB_4. (a) Top view and side view of the 2 × 2 optimized atomic structure. Beige, gray, and green represent B, Al, and Cr, respectively. (b) Electronic band structure with red inset box. (c) SOC band structure with red inset box. (d) Fat-bands projection on region with gap opening. Red and blue indicate contributions from Al3p and B2p orbitals, respectively. Green outlines represent contributions from Cr3d orbitals. Color bars show absolute orbital-projection values for each channel. (e) and (f) Spin-polarized spin-up and spin-down band structures. All panels follow the high-symmetry Γ–K–M–Γ k-point circuit.

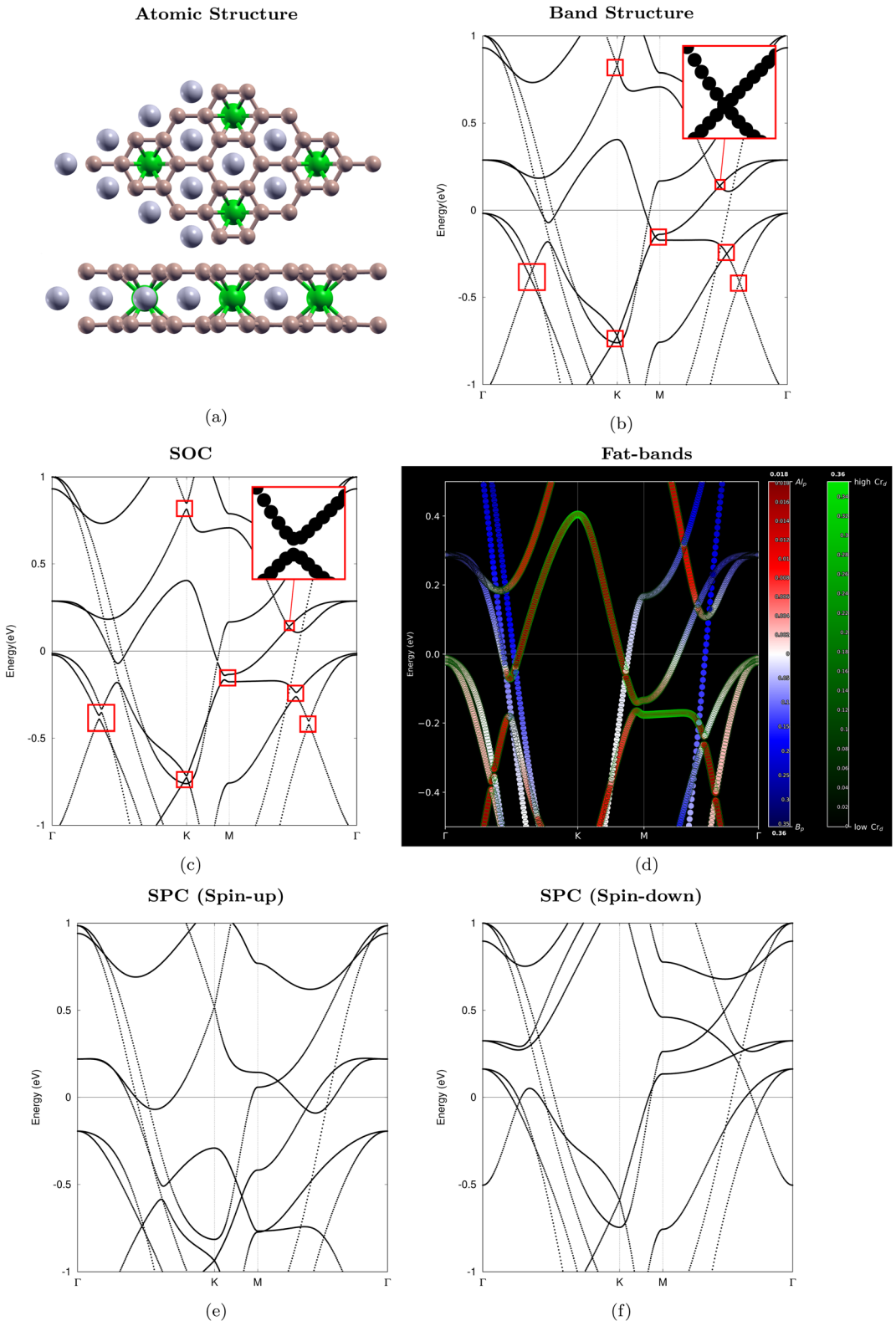

Fig. 14 Cr_{Al} in 2 × 2 AlB_4. (a) Top view and side view of the 2 × 2 optimized atomic structure. Beige, gray, and green represent B, Al, and Cr, respectively. (b) Electronic band structure with red inset box. (c) SOC band structure with red inset box. (d) Fat-bands projection on region with gap opening. Red and blue indicate contributions from Al3p and B2p orbitals, respectively. Green outlines represent contributions from Cr3d orbitals. Color bars show absolute orbital-projection values for each channel. (e) and (f) Spin-polarized spin-up and spin-down band structures. All panels follow the high-symmetry Γ–K–M–Γ k-point circuit.

A negligible 0.1% increase in lattice constant is calculated for AlB_4 Fe_B (Table 3). Below the Fermi level from M to Γ in the SOC band structure (Fig. 9(c)), a gap opens in the place of the crossing seen in Fig. 9(b), as indicated by the red inset box. In the bands near the gap, regions with greater Al3p contribution are shown to have bright green circle outlines, indicative of strong influences of the Fe3d. In addition, bar ticks show that the absolute weight of Al3p is very small near the Fermi level. Same with Al_2B_2 Fe_B, SPC produces no visible distinction between Fig. 9(e) and (f), thus the monolayer is not magnetic. The corresponding value from Table 3 supports this conclusion.

The relaxed in-plane lattice constant of AlB_4 Fe_{Al}, 11.221 bohr, is 1.41% smaller than that of the undoped supercell (Table 3). Akin to AlB_4 Mn_{Al}, introducing SOC effects results in the formation of numerous gaps in the band structure due to lowered symmetries (Fig. 10(c)). Qualitative results of the two monolayers are alike: strong influences of the Fe3d orbital in regions with greater Al3p contribution, B2p and Fe3d orbitals with greater absolute weights, and SPC bands revealing magnetism (Fig. 10(d)–(f) and Table 3).

Trends that can be concluded from Table 3 are very similar to those from Table 2. Substitutions on the Al site still have lower formation energies than those on the B site, and smaller in-plane lattice constants than the pristine monolayers. Thus, we arrive at the same conclusion that doping is easier to perform on the Al site.

3.4. Cr doped monolayers

Having found magnetic ground states for Mn and Fe, we now move on to Cr as our final dopant to examine whether the trend of dopant-induced magnetism persists, using the same settings and conventions.

The top and side views of the fully relaxed atomic structure of Al_2B_2 with substitutional Cr_B doping is shown in Fig. 11(a). The resulting lattice constant converges to 11.519 bohr, indicating a 3.48% increase (Table 4). The color green is used to indicate Cr atoms. From M to Γ, a gap opens up above the Fermi level in place of a crossing when SOC effects are introduced (Fig. 11(c)). The fat-bands plot of this monolayer reveals Cr3d to have the greatest weight around the gap, revealing its importance in producing this result. Fig. 11(e) and (f) are identical, and Table 4 reports its magnetic moment as 0, signifying that this monolayer is non-magnetic.

Comparable to the other Al_2B_2 monolayers with Al site doping, a band gap opens when SOC is applied, this time along the Γ–K path of the band structure (Fig. 12(c)). The dopant induces a minute, 0.70% increase in the lattice constant (11.054 bohr as seen from Table 4). The fat-bands plot of Fig. 12 shows that the dopant Cr contributes strongly to the mixing of orbitals responsible for breaking symmetry. The SPC band structures and Table 4 reveal the existence of magnetism (Fig. 12(e) and (f)).

A negligible 0.05% decrease in lattice parameters appears for AlB_4 with Cr_B doping (Table 4). A symmetry breaks above the Fermi level under the introduction of SOC effects to the band structure, this time from the K–M path (Fig. 13(c)). Fig. 13(d) show that the relative projections of Al3p orbital dominate near the gap, however Cr3d and B2p have much greater absolute weights. Green outlines of circles near the gap are indicative of the role of Cr3d in this outcome. Table 4, Fig. 13(e) and (f) once again show magnetism.

Finally, consistent with other AlB_4 monolayers with Al site doping, a number of different band crossings open under SOC effects for AlB_4 Cr_{Al} (Fig. 14(c)). An expected 1.42% decrease in lattice parameters in comparison to the pure material, from 11.369 to 11.209 bohr, is also present. Similarly, in all opened nodal points near the Fermi level, there exists strong influences of the Cr3d orbital, particularly in regions with greater Al3p contribution. B2p and Cr3d orbitals have greater absolute weights in these bands (Fig. 14(d)). Lastly, Table 4, Fig. 14(e) and (f) reveal magnetism.

4. Conclusion

In this study, we used first-principles calculations to investigate whether substitutional transition metal doping can induce magnetism in the lightweight, two-dimensional nodal line semimetal monolayers Al_2B_2 and AlB_4, while maintaining band features compatible with nontrivial topology. Our results reveal that Al site substitution is consistently more favorable energetically than B site substitution. We also discover the opening of crossings across all systems when spin–orbit coupling effects are introduced. Spin-polarized calculations reveal robust ferromagnetic ground states for Mn_B, Mn_{Al}, Fe_{Al}, and Cr_{Al} in 2×2 Al_2B_2, and for Mn_B, Mn_{Al}, Fe_{Al}, Cr_B, and Cr_{Al} in 2×2 AlB_4. Fat-bands analyses indicate strong interactions between the dopant and the host, relative to band openings. Taken together, these results suggest that the substitutional doping of these two monolayers could likely give rise to promising candidates for future spintronics applications. In future studies, we will specifically investigate topological properties, explore different host cell sizes, and incorporate a more comprehensive list of dopants to push for practical implementations of the monolayers in spintronics.

Conflicts of interest

There are no conflicts to declare.

Data availability

This study was carried out using publicly available data from ABINIT at https://github.com/orgs/abinit/repositories. All the data supporting this article are described within the text.

References

1 C. Marrows and B. Hickey, *Philos. Trans. R. Soc., A*, 2011, **369**(1948), 3027–3036.
2 D. J. Frank, *IBM J. Res. Dev.*, 2002, **46**, 235.
3 S. Wolf, D. Awschalom, R. Buhrman, J. Daughton, v. S. von Molnár, M. Roukes, A. Y. Chtchelkanova and D. Treger, *Science*, 2001, **294**, 1488.
4 A. Hirohata, K. Yamada, Y. Nakatani, I.-L. Prejbeanu, B. Diény, P. Pirro and B. Hillebrands, *J. Magn. Magn. Mater.*, 2020, **509**, 166711.

5 L. Guo, X. Gu, X. Zhu and X. Sun, *Adv. Mater.*, 2019, **31**, 1805355.
6 I. Žutić, J. Fabian and S. D. Sarma, *Rev. Mod. Phys.*, 2004, **76**, 323.
7 H. X. Tang, F. Monzon, F. J. Jedema, A. T. Filip, B. J. van Wees and M. L. Roukes, in *Semiconductor Spintronics and Quantum Computation*, Springer, 2002, pp. 31–92.
8 M. N. Baibich, J. M. Broto, A. Fert, F. N. Van Dau, F. Petroff, P. Etienne, G. Creuzet, A. Friederich and J. Chazelas, *Phys. Rev. Lett.*, 1988, **61**, 2472.
9 J. Barnaś, A. Fuss, R. Camley, P. Grünberg and W. Zinn, *Phys. Rev. B:Condens. Matter Mater. Phys.*, 1990, **42**, 8110.
10 S. A. Wolf, A. Y. Chtchelkanova and D. M. Treger, *IBM J. Res. Dev.*, 2006, **50**, 101.
11 J. Lu, E. Chen, M. Kabir, M. Stan and S. Wolf, *Int. Mater. Rev.*, 2016, **61**, 456.
12 J. S. Moodera, L. R. Kinder, T. M. Wong and R. Meservey, *Phys. Rev. Lett.*, 1995, **74**, 3273.
13 M. Hellenbrand, I. Teck and J. L. MacManus-Driscoll, *MRS Commun.*, 2024, **14**, 1099.
14 T. Dietl and H. Ohno, *Rev. Mod. Phys.*, 2014, **86**, 187.
15 T. Endoh, *Mater. Lett.*, 2024, **6**, 400.
16 D. H. Kang and M. Shin, *Sci. Rep.*, 2021, **11**, 22842.
17 H. Kim, K.-W. Kwon and Y. Seo, *Electronics*, 2024, **13**, 3498.
18 T. Lee, K. Yamane, Y. Otani, D. Zeng, J. Kwon, J. Lim, V. Naik, L. Hau, R. Chao, N. Chung, *et al.*, in *2020 IEEE International Electron Devices Meeting (IEDM)*, IEEE, 2020, pp. 11–16.
19 Y. Seo, X. Fong and K. Roy, *IEEE Trans. Electron Devices*, 2014, **62**, 554.
20 C. Lin, S. Kang, Y. Wang, K. Lee, X. Zhu, W. Chen, X. Li, W. Hsu, Y. Kao, M. Liu, *et al.*, in *2009 IEEE International Electron Devices Meeting (IEDM)*, IEEE, 2009, pp. 1–4.
21 K. C. Chun, H. Zhao, J. D. Harms, T.-H. Kim, J.-P. Wang and C. H. Kim, *IEEE J. Solid State Circ.*, 2012, **48**, 598.
22 Z. Bian, X. Hong, Y. Guo, L. Naviner, W. Ge and H. Cai, *Micromachines*, 2021, **12**, 551.
23 X. Jia and Y. Jiang, *AIP Adv.*, 2024, **14**, 025305.
24 J. Cui, K.-X. Zhang and J.-G. Park, *Adv. Electron. Mater.*, 2024, **10**, 2400041.
25 V. Nguyen, S. Rao, K. Wostyn and S. Couet, *npj Spintronics*, 2024, **2**, 48.
26 V. H. Guarochico-Moreira, J. L. Sambricio, K. Omari, C. R. Anderson, D. A. Bandurin, J. C. Toscano-Figueroa, N. Natera-Cordero, K. Watanabe, T. Taniguchi, I. V. Grigorieva, *et al.*, *Nano Lett.*, 2022, **22**, 935.
27 C. Niu, G. Qiu, Y. Wang, P. Tan, M. Wang, J. Jian, H. Wang, W. Wu and P. D. Ye, *Nano Lett.*, 2023, **23**, 8445.
28 B. A. Bernevig, C. Felser and H. Beidenkopf, *Nature*, 2022, **603**, 41.
29 M. R. K. Akanda, *AIP Adv.*, 2020, **10**, 095222.
30 S. Nakatsuji, *AAPPS Bull.*, 2022, **32**, 25.
31 M. Guimarães, P. Zomer, J. Ingla-Aynés, J. Brant, N. Tombros and B. Wees, *Phys. Rev. Lett.*, 2014, **113**, 086602.
32 A. Avsar, J. Y. Tan, T. Taychatanapat, J. Balakrishnan, G. Koon, Y. Yeo, J. Lahiri, A. Carvalho, A. Rodin, E. O'farrell, *et al.*, *Nat. Commun.*, 2014, **5**, 4875.
33 T. Wang, M. Vila, M. P. Zaletel and S. Chatterjee, *Phys. Rev. Lett.*, 2024, **132**, 116504.
34 K. F. Mak, K. He, J. Shan and T. F. Heinz, *Nat. Nanotechnol.*, 2012, **7**, 494.
35 B. A. Bernevig and S.-C. Zhang, *Phys. Rev. Lett.*, 2006, **96**, 106802.
36 J. Maciejko, T. L. Hughes and S.-C. Zhang, *Annu. Rev. Condens. Matter Phys.*, 2011, **2**, 31.
37 S. Karki Chhetri, R. Basnet, J. Wang, K. Pandey, G. Acharya, M. R. U. Nabi, D. Upreti, J. Sakon, M. Mortazavi and J. Hu, *Phys. Rev. B*, 2024, **109**, 184429.
38 J. Zou, Z. He and G. Xu, *npj Comput. Mater.*, 2019, **5**, 96.
39 M. Piquemal-Banci, R. Galceran, F. Godel, S. Caneva, M.-B. Martin, R. S. Weatherup, P. R. Kidambi, K. Bouzehouane, S. Xavier, A. Anane, *et al.*, *ACS Nano*, 2018, **12**, 4712.
40 Y. Wang, X. Xu, W. Ji, S. Li, Y. Li and X. Zhao, *npj Comput. Mater.*, 2023, **9**, 223.
41 A. Avsar, I. J. Vera-Marun, J. Y. Tan, G. K. W. Koon, K. Watanabe, T. Taniguchi, S. Adam and B. Özyilmaz, *NPG Asia Mater.*, 2016, **8**, e274.
42 K. S. Novoselov, A. K. Geim, S. V. Morozov, D.-e. Jiang, Y. Zhang, S. V. Dubonos, I. V. Grigorieva and A. A. Firsov, *Science*, 2004, **306**, 666.
43 X. Zhang, X. Wang, T. He, L. Wang, W.-W. Yu, Y. Liu, G. Liu and Z. Cheng, *Sci. Bull.*, 2023, **68**, 2639.
44 A. Kara, H. Enriquez, A. P. Seitsonen, L. L. Y. Voon, S. Vizzini, B. Aufray and H. Oughaddou, *Surf. Sci. Rep.*, 2012, **67**, 1.
45 K. Zhang, Y. Feng, F. Wang, Z. Yang and J. Wang, *J. Mater. Chem. C*, 2017, **5**, 11992.
46 S. Manzeli, D. Ovchinnikov, D. Pasquier, O. V. Yazyev and A. Kis, *Nat. Rev. Mater.*, 2017, **2**, 1.
47 J. Liu, J. Hu, Q. Zhang, D. Graf, H. B. Cao, S. Radmanesh, D. Adams, Y. Zhu, G. Cheng, X. Liu, *et al.*, *Nat. Mater.*, 2017, **16**, 905.
48 Z. Fei, B. Huang, P. Malinowski, W. Wang, T. Song, J. Sanchez, W. Yao, D. Xiao, X. Zhu, A. F. May, *et al.*, *Nat. Mater.*, 2018, **17**, 778.
49 E. Gati, S. L. Bud'ko, L.-L. Wang, A. Valadkhani, R. Gupta, B. Kuthanazhi, L. Xiang, J. M. Wilde, A. Sapkota, Z. Guguchia, *et al.*, *Phys. Rev. B*, 2021, **104**, 155124.
50 K. Kim, J. Seo, E. Lee, K.-T. Ko, B. Kim, B. G. Jang, J. M. Ok, J. Lee, Y. J. Jo, W. Kang, *et al.*, *Nat. Mater.*, 2018, **17**, 794.
51 S. Abedi, E. T. Sisakht, S. J. Hashemifar, N. G. Cherati, I. A. Sarsari and F. M. Peeters, *Nanoscale*, 2022, **14**, 11270.
52 Y. Zhao, C. Lian, S. Zeng, Z. Dai, S. Meng and J. Ni, *Phys. Rev. B*, 2019, **100**, 094516.
53 X. Zhang, K.-H. Jin, J. Mao, M. Zhao, Z. Liu and F. Liu, *npj Comput. Mater.*, 2021, **7**, 44.
54 R.-F. Zou, X.-J. Ye, X.-H. Zheng, R. Jia and C.-S. Liu, *Phys. Chem. Chem. Phys.*, 2023, **25**, 28814.
55 S. Baidya, J. Yu and C. H. Kim, *Phys. Rev. B*, 2018, **98**, 155148.
56 F. Wang, Y. Zhang, W. Yang, J. Zhang, H. Zhang and X. Xu, *Phys. Rev. B*, 2023, **107**, 174405.
57 M. Fang, S. Chen, C. Tang, Z. Tang, M.-Y. Choi, J. H. Jang, H.-S. Chung, M. N. Nair, W. Jin, and E.-H. Yang, *arXiv*,

2024, preprint, arXiv:2409.11222, DOI: 10.48550/arXiv.2409.11222.
58 Q. Cheng, Z. Yan, W. Song, J. Kong, D. Li, W. Xu, Y. Xie, X. Liang and Z. Zhao, *Phys. Chem. Chem. Phys.*, 2023, **25**, 29633.
59 Y. Wu, D. Li, C.-L. Wu, H. Y. Hwang and Y. Cui, *Nat. Rev. Mater.*, 2023, **8**, 41.
60 L. Zhang, Y. Zhao, Y. Liu and G. Gao, *Nanoscale*, 2023, **15**, 18910–18919.
61 L. Zhang, Y. Liu, M. Wu and G. Gao, *Adv. Funct. Mater.*, 2025, **35**, 2417857.
62 S. Fu, K. Kang, K. Shayan, A. Yoshimura, S. Dadras, X. Wang, L. Zhang, S. Chen, N. Liu, A. Jindal, *et al.*, *Nat. Commun.*, 2020, **11**, 2034.
63 M. Fang and E.-H. Yang, *Materials*, 2023, **16**, 3701.
64 Z. Li, X. Guan, G. Pandey, S. Chahal, A. Bandyopadhyay, K. Awasthi, P. Kumar and A. Vinu, *Small*, 2024, **20**, 2307610.
65 X. Gonze, B. Amadon, P.-M. Anglade, J.-M. Beuken, F. Bottin, P. Boulanger, F. Bruneval, D. Caliste, R. Caracas, M. Cote, *et al.*, *Comput. Phys. Commun.*, 2009, **180**, 2582.
66 P. Blochl, *Phys. Rev. B:Condens. Matter Mater. Phys.*, 1994, **50**, 17953.
67 N. A. W. Holzwarth, A. R. Tackett and G. E. Matthews, *Comput. Phys. Commun.*, 2001, **135**, 329.
68 S. Zhang and J. E. Northrup, *Phys. Rev. B:Condens. Matter Mater. Phys.*, 1991, **67**, 2339.
69 C. Freysoldt, B. Grabowski, T. Hickel, J. Neugebauer, G. Kresse, A. Janotti and C. G. Van de Walle, *Rev. Mod. Phys.*, 2014, **86**, 253.
70 H.-P. Komsa and A. V. Krasheninnikov, *Phys. Rev. B:Condens. Matter Mater. Phys.*, 2015, **91**, 125304.
71 X.-B. Wang, X.-M. Ma, E. Emmanouilidou, B. Shen, C.-H. Hsu, C.-S. Zhou, Y. Zuo, R.-R. Song, S.-Y. Xu, G. Wang, *et al.*, *Phys. Rev. B*, 2017, **96**, 161112.
72 D. Shao, T. Chen, Q. Gu, Z. Guo, P. Lu, J. Sun, L. Sheng and D. Xing, *Sci. Rep.*, 2018, **8**, 1467.
73 T.-R. Chang, I. Pletikosic, T. Kong, G. Bian, A. Huang, J. Denlinger, S. K. Kushwaha, B. Sinkovic, H.-T. Jeng, T. Valla, *et al.*, *Adv. Sci.*, 2019, **6**, 1800897.